

## CFHT MegaCam Two Deep Fields Imaging Survey (2DFIS) II: Decoding the Lensing Profile of a "Rotating" Cluster with Deep CFHT Imaging

YICHENG LI,<sup>1,2</sup> LIPING FU,<sup>1,3</sup> WENTAO LUO,<sup>4,5</sup> BINYANG LIU,<sup>6</sup> WEI DU,<sup>1</sup> MARTIN KILBINGER,<sup>7</sup> CALUM MURRAY,<sup>7</sup> CHRISTOPHER J. MILLER,<sup>8,9</sup> RAY WANG,<sup>10</sup> DAVID TURNER,<sup>11,12</sup> LANCE MILLER,<sup>13</sup> DEZI LIU,<sup>14</sup> MARIO RADOVICH,<sup>15</sup> JEAN-PAUL KNEIB,<sup>16</sup> HUANYUAN SHAN,<sup>2</sup> KAIWEN MAI,<sup>1</sup> ZICHENG WANG,<sup>1</sup> AND HAORAN ZHAO<sup>1</sup>

<sup>1</sup>*Shanghai Key Lab for Astrophysics, Shanghai Normal University, Shanghai 200234, China*

<sup>2</sup>*Shanghai Astronomical Observatory, Chinese Academy of Sciences, Shanghai 200030, China*

<sup>3</sup>*Center for Astronomy and Space Sciences, China Three Gorges University, Yichang 443000, China*

<sup>4</sup>*School of Aerospace Information and Technology, Hefei Institute of Technology, Hefei, Anhui 230031, China*

<sup>5</sup>*Department of Astronomy, School of Physical Sciences, University of Science and Technology of China, Hefei, Anhui 230026, China*

<sup>6</sup>*Purple Mountain Observatory, Chinese Academy of Sciences, Nanjing, Jiangsu 210008, China*

<sup>7</sup>*Université Paris-Saclay, Université Paris Cité, CEA, CNRS, AIM, 91191, Gif-sur-Yvette, France*

<sup>8</sup>*Department of Astronomy, University of Michigan, Ann Arbor, MI 48109, USA*

<sup>9</sup>*Department of Physics, University of Michigan, Ann Arbor, MI 48109, USA*

<sup>10</sup>*Department of Physics and Astronomy, Michigan State University, East Lansing, MI 48824, USA*

<sup>11</sup>*Center for Space Sciences and Technology, University of Maryland, Baltimore County, Baltimore, MD 21250, USA*

<sup>12</sup>*High Energy Astrophysics Science Archive Research Center, Greenbelt, MD 20771, USA*

<sup>13</sup>*Department of Physics, Oxford University, Keble Road, Oxford OX1 3RH, UK*

<sup>14</sup>*South-Western Institute For Astronomy Research, Yunnan University, Kunming 650500, China*

<sup>15</sup>*INAF - Osservatorio Astronomico di Padova, via dell'Osservatorio 5, 35122 Padova, Italy*

<sup>16</sup>*École Polytechnique Fédérale de Lausanne, 1015 Lausanne, Switzerland*

Submitted to ApJS

### ABSTRACT

We present a multi-wavelength analysis of the galaxy cluster RXCJ0110.0+1358 ( $z = 0.058$ ), a rotating cluster candidate, combining deep CFHT imaging, SDSS photometry, spectroscopic redshifts, and XMM-Newton X-ray observations. We find a notable discrepancy between the optical and X-ray views: while optical data reveal a pronounced bimodal galaxy distribution with significant kinematic substructure signatures, the X-ray emission exhibits a single, smoothly extended component centered on the BCG. Our weak lensing analysis resolves this discrepancy by revealing that the mass is predominantly concentrated in the southeast ( $\log M_{200}/M_{\odot} = 14.04^{+0.24}_{-0.40}$ ), while the northwestern substructure has a negligible mass ( $\sim 10^{13} M_{\odot}$ ). This immense mass disparity rules out the dynamical possibility of a rotating system. We demonstrate that the apparent optical bimodality arises from the projection of a filament, which led optical group-finding algorithms to misclassify these galaxies as cluster members. This contamination creates a spurious substructure that mimics a rotation signal and leads to an overestimation of the luminosity-based halo mass, resolving the observed inconsistencies.

*Keywords:* Weak gravitational lensing (1797) — Galaxy clusters (584)

### 1. INTRODUCTION

Galaxy clusters are the largest self-gravitating systems in the universe, consisting of tens to thousands of galaxies, the intracluster medium (ICM), and a dominant

Corresponding author: Liping Fu  
 fuliping@shnu.edu.cn

Corresponding author: Wentao Luo  
 wtluo@ustc.edu.cn

dark matter halo, with typical masses ranging from  $10^{14}$  to  $10^{15} M_{\odot}$ . Representing the latest stage of hierarchical structure formation, galaxy clusters function as potent cosmological probes (Kravtsov & Borgani 2012; Allen et al. 2011).

The mass of a galaxy cluster is a crucial probe for constraining cosmological models, necessitating precise measurement. Various techniques have been developed for mass estimation, including the Sunyaev-Zel'dovich (SZ) effect (Bleem et al. 2015), the temperature of the intracluster medium (ICM) from X-ray emission (Ettori et al. 2013), the dynamics of satellite member galaxies (Heisler et al. 1985), and gravitational lensing (Kneib & Natarajan 2011). Notably, gravitational lensing is unique among these methods as it infers the total mass distribution directly, without relying on assumptions about the dynamical state or baryonic physics of the cluster. This is achieved by measuring the coherent distortion (shear) of background galaxy images, which arises from the deflection of light by the gravitational potential of the foreground cluster.

An active area of research is the potential for galaxy clusters to exhibit coherent rotation. In the standard  $\Lambda$ CDM paradigm, halos are expected to acquire a net angular momentum from tidal torques exerted by the surrounding large-scale structure during their formation (Peebles 1969). However, observational claims of rotation are often based on kinematic signatures that can be ambiguous. These signatures include velocity gradients in the line-of-sight velocities of member galaxies (Hwang & Lee 2007; Tovmassian 2015; Manolopoulou & Plionis 2017; Bilton et al. 2019) or dipole patterns in kinetic Sunyaev-Zel'dovich (kSZ) effect maps (Chluba & Mannheim 2002; Cooray & Chen 2002). Such features may instead be transient phenomena caused by ongoing mergers, oscillating substructures, or simply the chance projection of unbound galaxy groups along the line-of-sight (Manolopoulou & Plionis 2017). Differentiating between a dynamically settled, rotating halo and a complex, merging system is therefore critical for understanding cluster assembly. Evidence from both simulations and observations remains contested, highlighting the need for multi-wavelength analysis (Baldi et al. 2018; Altamura et al. 2023; Tang et al. 2025).

Distinguishing between these physical scenarios requires a direct probe of the underlying matter distribution, which motivates the use of weak gravitational lensing. A weak lensing mass map can reveal the fundamental morphology of the potential well. A disturbed, multi-peaked mass distribution would strongly indicate a merger, suggesting any kinematic signal is transient. Conversely, a singular, relatively symmetric mass peak

located near the kinematic rotation center would be more consistent with a virialized halo where coherent rotation might be present. To this end, we initiated a program to map the mass of clusters identified as rotation candidates. From the SDSS DR7 (Abazajian et al. 2009) group catalog (Wang et al. 2014; Yang et al. 2007), we selected 33 clusters with potential rotational or merging features, each comprising more than 50 member galaxies and possessing a mass exceeding  $10^{14} M_{\odot}$ . Specifically, these candidates are characterized by a sinusoidal variation in the mean redshift of member galaxies on opposite sides of the luminosity center as a function of the position angle of the dividing axis.

In this study, we present a detailed weak lensing analysis of one such candidate, RXCJ0110.0+1358, using deep observations from CFHT MegaCam (Boulade et al. 2003). This cluster is a particularly compelling candidate as it exhibits clear signs of a dynamically complex state. Optically, its galaxy distribution is bimodal, with two distinct luminosity centers in the southeast and northwest, resulting in a significant offset of approximately 10 arcmin between the luminosity-weighted center and the Brightest Cluster Galaxy (BCG). By reconstructing its 2D mass map, we can directly assess its dynamical state and investigate the physical origin of its previously reported rotational signature. Our analysis reveals a single, dominant mass peak with  $\log(M_{200}/M_{\odot}) = 14.04^{+0.24}_{-0.40}$  which is spatially coincident with the cluster's BCG. This finding, combined with our kinematic and X-ray analysis, suggests that the previously reported rotation signal is likely an artifact, caused by the misidentification of member galaxies belonging to a projected filament.

The remainder of this paper is structured as follows. Section 2 provides an overview of the galaxy cluster data, the X-ray observations obtained from XMM-Newton, CFHT imaging, as well as details of our data reduction procedures. In Section 4, we summarize the shear measurement techniques used. Section 5 is dedicated to the presentation of our reconstructed mass map, which is then compared to the ELUCID simulation data. Finally, Section 6 provides a summary of the findings.

Throughout this work, we adopt the AB magnitude system and a flat  $\Lambda$ CDM cosmology characterized by  $\Omega_m = 0.3$ ,  $\Omega_{\Lambda} = 0.7$ , and  $H_0 = 70 \text{ km s}^{-1} \text{ Mpc}^{-1}$ . At the cluster redshift of  $z_{\text{cl}} = 0.05828$ ,  $1'$  corresponds to  $\sim 71$  kpc. The adopted cluster center is  $\text{ra} = 17.51^\circ$ ,  $\text{dec} = 13.98^\circ$  (J2000). The notation  $M_{200}$  is utilized to denote the mass for which the mean density enclosed within a sphere of radius  $R_{200}$  is 200 times the critical density of the universe.

## 2. DATA

The galaxy cluster RXCJ0110.0+1358 is selected from the group catalog of Wang et al. (2014). This catalog is built upon data from the ROSAT All-Sky Survey (Voges et al. 1999, RASS), which provides broad-band X-ray imaging and the optical group catalog of SDSS DR7 (Yang et al. 2012, hereafter Y12). The optical galaxy clusters are identified using model magnitudes and a modified halo-based group finder developed by Yang et al. (2005). In the catalog, cluster masses are estimated based on a calibration between mass and the stellar content of member galaxies. The logarithmic halo mass derived from measurements of the mass-to-light ratio is  $\log(M/M_{\odot}) = 14.43$ .

We utilize the group catalog constructed by Yang et al. (2012), which selects galaxies with extinction-corrected  $r$ -band magnitudes  $m_r < 17.72$  and a redshift completeness qualification of  $C > 0.7$ . Based on these criteria, the cluster comprises 71 member galaxies. Of these, 56 have spectroscopic redshifts from SDSS DR7, while the remaining members are assigned the redshift of their nearest neighbor in the Y12 catalog. The cluster center is defined by the position of the BCG, which is identified as the brightest galaxy in the  $r$ -band with a spectroscopic redshift consistent with the cluster rest frame, is located at coordinates  $\text{ra} = 17.51321^{\circ}$ ,  $\text{dec} = 13.97816^{\circ}$ , with a redshift of  $z_{\text{cl}} = 0.05828$ . In contrast, the luminosity-weighted center cataloged in Y12, which derives luminosities from absolute magnitudes including  $K$ -corrections and evolutionary corrections, is positioned at  $\text{ra} = 17.44393^{\circ}$ ,  $\text{dec} = 14.14400^{\circ}$ , which is displaced by  $\sim 11$  arcmin from the BCG position with  $z'_{\text{cl}} = 0.05981$ . This discrepancy arises due to the cluster's bimodal luminosity distribution, characterized by distinct southeastern and northwestern components.

The regions of these two luminosity components were observed by XMM-Newton in two separate pointings, ObsID 0503600701 (Arnold et al. 2009) and 0693221601 (Yershov 2014), which covers the southeastern and northwestern regions, respectively.

### 2.1. X-ray Data

We retrieved XMM-Newton observations from the XMM-Newton Science Archive (XSA<sup>1</sup>), including calibrated event files, exposure-corrected images, and source region files. Figure 1 presents the co-added X-ray image in the 0.5–2.0 keV band, overlaid with optical  $r$ -band luminosity contours. The X-ray emission is spatially consistent with the  $r$ -band luminosity map in the southeast-

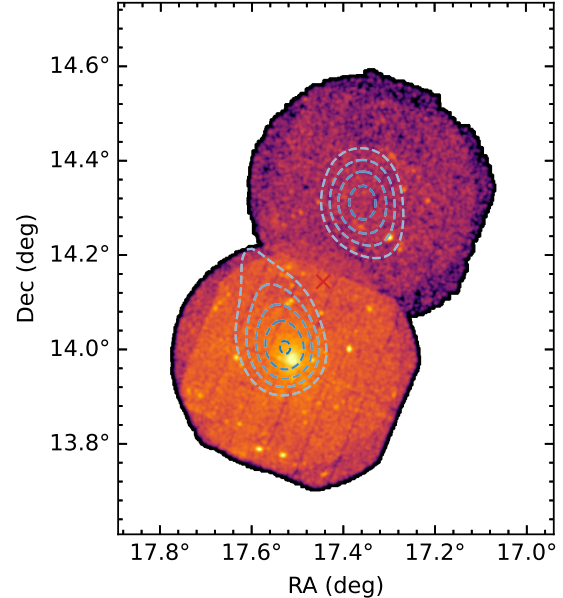


**Figure 1.** XMM-Newton image in the 0.5–2.0 keV band. Dashed contours show the optical  $r$ -band galaxy luminosity.

ern part of the cluster, where an extended X-ray source is clearly aligned with the optical luminosity peak. In contrast, no significant extended X-ray emission is detected at the location of the northwestern optical peak.

We start with the calibrated event files from the Pipeline Processing System (PPS) and use SAS v22.0.0 for event selection. Following Gu et al. (2012), we applied a selection with  $\text{FLAG} = 0$ ,  $\text{PATTERN} \leq 12$  for MOS cameras and  $\text{PATTERN} \leq 4$  for pn camera, and examined light curves extracted in 10.0 – 14.0 keV from the full frame, and 1.0 – 5.0 keV from source-free regions, time intervals for which the count rate exceeds a  $2\sigma$  limit above the quiescent mean value are rejected. The final effective exposure times are 16 ks, 16 ks, and 8 ks for MOS1, MOS2 and pn, respectively.

To estimate the cluster mass, we adopt the core-included  $M_{200} - T_X$  scaling relation derived by Umetsu et al. (2020). To ensure consistency with their calibration, we extract the X-ray spectrum following their specific definition: utilizing the 0.4–11.0 keV energy band within a central circular aperture of 300 kpc. At the cluster redshift ( $z = 0.058$ ), this physical radius corresponds to an angular radius of  $261''$ . All point sources within this region were excluded, and a concentric annulus with an inner radius of  $650''$  and an outer radius of  $700''$  was used to estimate the local background.

The spectrum was fitted using XSPEC (v12.14.1) with model  $\text{TBABS} * \text{APEC}$ . This analysis yields a best-fit core-included temperature of  $T_{300\text{kpc}} = 2.86 \pm 0.12$  keV

<sup>1</sup> <https://www.cosmos.esa.int/web/xmm-newton/xsa>

with a C-statistic of 489.19 for 411 degrees of freedom. We then calculate the mass using the scaling relation from Umetsu et al. (2020):

$$E(z)M_{200} = (4.58 \pm 0.70) \times 10^{13} M_{\odot} \times \left( \frac{T_{300\text{kpc}}}{1 \text{ keV}} \right)^{3/2}, \quad (1)$$

where  $E(z) = H(z)/H_0$  describes the evolution of the Hubble parameter. Substituting our measured temperature into this relation, we obtain a mass of  $\log(M_{200}/M_{\odot}) = 14.33 \pm 0.07$ . It is important to note that since the X-ray emission is concentrated solely on the southeastern component, this value estimates the mass of the main cluster halo. This value is slightly lower than the mass estimate from the Y12 catalog, but remains consistent within  $1\sigma$  uncertainties.

## 2.2. CFHT Imaging and Data Reduction

The galaxy cluster RXCJ0110.0+1358 was observed with the CFHT MegaCam on October 1, 2 and 4, 2020 (Proposal ID: 22BD07; PI W. Luo). MegaCam provides a  $\sim 1 \text{ deg}^2$  field of view, which is large enough to cover the majority of the cluster's member galaxies in a single pointing. The total integration times of the  $u$ ,  $g$ ,  $r$  and  $i$  bands are 3840 s, 1680 s, 3680 s, and 3840 s, respectively, reaching a  $5\sigma$  point-source limiting magnitude of approximately 26.0 mag in each band. A dithering strategy was applied to fill the CCD gaps. We used  $r$ -band images for the following weak lensing analysis.

A comprehensive reduction of the data was previously provided in Liu et al. (2025, submitted) using the LSST Science Pipelines. Here, we re-process the raw exposures with an independent workflow to ensure full compatibility with the shear-measurement tools employed in this study. This parallel reduction is complementary to Liu et al. (2025, submitted) and is optimized for weak-lensing shape measurements rather than general-purpose catalog production. For each exposure, we perform cosmic ray rejection using the Python package `ccdproc` (Craig et al. 2017) and sky background subtraction using `photutils` (Bradley et al. 2024). Astrometric calibration is carried out using software `SCAMP` (Bertin 2006) with an external reference catalog from GAIA-DR2 (Gaia Collaboration et al. 2018). The calibrated exposures were then coadded with `SWarp` (Bertin 2010) for the following processing.

Bad pixels and edges of images are masked with a flat-field image. Masks of saturated stars are created by first selecting pixels close to the saturation threshold and then using a segmentation map that includes saturated pixels to mark saturated stars. Satellite traces are identified and masked by inspecting residual images created from subtracting individual exposures from the

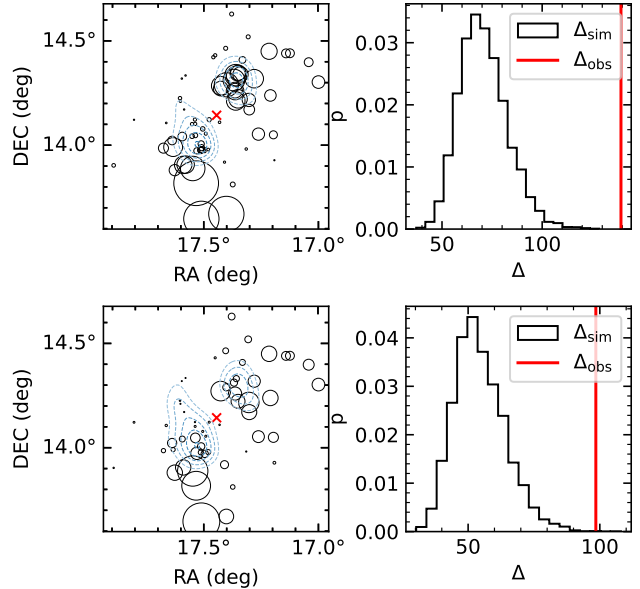


**Figure 2.** Results of the substructure test. The top and bottom rows correspond to Case 1 (all members) and Case 2 spectroscopic members only, respectively. *Left panels*: Spatial distribution of the  $\delta$  statistic. The radius of each circle scales with  $e^{\delta_i}$ . Blue contours trace the galaxy luminosity map, and the red cross marks the luminosity-weighted center. *Right panels*: Distribution of the cumulative  $\Delta_{\text{sim}}$  statistic derived from Monte Carlo realizations. The vertical red line indicates the observed  $\Delta$  value calculated from the data.

final coadd. Given the limited number of dithered exposures, bright star halos and scattered light artifacts were not fully suppressed by the coaddition process and were subsequently masked manually using `DS9`. The source catalog is then created using `SExtractor` (Bertin & Arnouts 1996), 163,853 objects are detected in  $r$ -band coadded image when no selection is applied.

## 3. DYNAMICS ANALYSIS

### 3.1. Tests of Substructure

As mentioned in Sect. 2, there is a  $\sim 11$  arcmin offset between the BCG and the luminosity-weighted center, which suggests the presence of significant substructure. Therefore, following Bilton et al. (2019) (hereafter B19) and Kang et al. (2024), we applied the  $\delta$ -test (Dressler & Shectman 1988) to investigate possible substructures, we approximate the line-of-sight velocity as  $v = cz$ , where  $z$  is the redshift of galaxies from Y12 catalog. Given that the cluster catalog contains both spectroscopic and non-spectroscopic redshifts, we perform the analysis for two scenarios. For clarity, we define Case 1 as including all 71 identified members, and Case 2 as restricted to the 56 members with spectroscopic redshifts.

The results for Case 2 are presented within parentheses below.

The  $\delta$  – test quantifies the local deviation from the global mean velocity and velocity dispersion for each galaxy via the  $\delta_i$  statistic, which is defined as:

$$\delta_i^2 = \left( \frac{N_{\text{nn}} + 1}{\sigma_{\text{glob}}^2} \right) [(\bar{v}_{\text{local}} - \bar{v}_{\text{glob}})^2 + (\sigma_{\text{local}} - \sigma_{\text{glob}})^2], \quad (2)$$

where  $\bar{v}$  and  $\sigma$  are the mean velocity and velocity dispersion, respectively. The subscript "local" denotes the quantities computed from a subsample of  $N_{\text{nn}}$  nearest neighbors galaxies. We use  $N_{\text{nn}} = \sqrt{N_{\text{glob}}}$  as suggested in B19, which is 9 for Case 1 (and 8 for Case 2) in this work. Using the line-of-sight velocities, we calculated the local and global statistics; the results are presented in the left panels of Figure 2. Each circle represents a galaxy, with its radius proportional to  $e^{\delta_i}$ . Consequently, a clustering of large circles indicates the presence of potential substructures. As illustrated in the left panels of Figure 2, a clear concentration of galaxies with large  $\delta_i$  values is observed in the northwestern part of the cluster, coinciding with the secondary luminosity peak.

To quantify the statistical significance of these substructures, we calculate the cumulative statistic  $\Delta$  defined as the sum of  $\delta_i$  over all member galaxies. We perform 10,000 Monte Carlo realizations by randomly permuting the galaxy velocities while preserving their spatial coordinate. The resulting distribution of the simulated statistics, denoted as  $\Delta_{\text{sim}}$  is shown in the right panel of Figure 2. Notably, none of the 10,000 simulations produced a  $\Delta_{\text{sim}}$  value as large as the one observed ( $\Delta_{\text{obs}}$ ), implying a significance level of  $p\text{-value} < 0.0001$ . This result strongly rejects the null hypothesis of a single Gaussian velocity distribution, revealing significant signals of kinematic substructure.

### 3.2. Tests of Rotation

Following the method proposed by [Manolopoulou & Plionis \(2017\)](#) (hereafter MP17), we searched for rotation signals by analyzing the spatial distribution of galaxy velocities. We calculated the rest-frame line-of-sight velocity,  $v_{\text{los}}$ , for each member galaxy as ([Danese et al. 1980](#)):

$$v_{\text{los}} = c \times \frac{z_{\text{gal}} - z'_{\text{cl}}}{1 + z'_{\text{cl}}}, \quad (3)$$

where  $z_{\text{gal}}$  is the galaxy redshift and  $z'_{\text{cl}}$  is the redshift of the cluster's rotation center. To detect rotation, we defined an axis passing through this center on the sky plane, which divides the member galaxies into two subsamples. We then calculated the difference in the mean

line-of-sight velocities between these two groups, defined as  $\Delta\bar{v}_{\text{los}} = \bar{v}_{\text{los},1} - \bar{v}_{\text{los},2}$ , where  $\bar{v}_{\text{los},1}$  and  $\bar{v}_{\text{los},2}$  are the mean velocities of the two groups. The velocity difference  $\Delta\bar{v}_{\text{los}}$  varies with the position angle ( $\theta$ ). For a rotating galaxy cluster, this variation is expected to exhibit a sinusoidal pattern. The amplitude of this variation represents the projected rotational velocity, and the position angle yielding the maximum velocity difference corresponds to the projection of the rotation axis on the sky plane.

To further distinguish whether a cluster is rotating, MP17 introduced the ideal rotation curve and the random rotation curve. The ideal rotation curve represents a perfect rotation scenario. It is derived by assuming that the fitted rotation axis is the true axis. For this model, the line-of-sight velocity of each galaxy is set to a constant value: half of the rotation velocity. A positive or negative sign is then assigned to this value depending on which side of the axis the galaxy lies. The random curve represents the null hypothesis where no coherent rotation exists. It is generated by repeatedly and randomly shuffling the full set of galaxy velocities and reassigning them to the fixed galaxy positions on the sky. This process destroys any real kinematic correlation with position while preserving the overall velocity distribution.

Following the methodology of MP17, we quantify rotational significance using three statistical indicators: the reduced chi-square of the ideal model ( $\chi_{\text{id}}^2/\text{dof}$ ), the ratio of the ideal-to-random chi squares ( $\chi_{\text{id}}^2/\chi_{\text{rd}}^2$ ), and the Kolmogorov-Smirnov (KS) test probability ( $P_{\text{KS}}$ ). The  $\chi^2$  statistics are defined as:

$$\chi_{\text{id}}^2 = \sum \frac{(\Delta\bar{v}_\theta - \Delta\bar{v}_{\text{id},\theta})^2}{\sigma_\theta^2 + \sigma_{\text{id},\theta}^2}, \quad (4)$$

and

$$\chi_{\text{rd}}^2 = \sum \frac{(\Delta\bar{v}_\theta - \langle \Delta\bar{v}_{\text{rd},\theta} \rangle)^2}{\sigma_\theta^2 + \sigma_{\text{rd},\theta}^2}, \quad (5)$$

where  $\Delta\bar{v}_\theta$  is  $\Delta\bar{v}_{\text{los}}$  at position angle of  $\theta$ ,  $\Delta\bar{v}_{\text{id},\theta}$  denotes the  $\Delta\bar{v}_\theta$  from ideal rotation curve, and  $\langle \Delta\bar{v}_{\text{rd},\theta} \rangle$  represents the mean value derived from the ensemble of random realizations,  $\sigma_\theta$  is the uncertainty at angle  $\theta$ , obtained using

$$\sigma_\theta^2 = \left( \frac{\sigma_{v1}}{\sqrt{n_1}} \right)^2 + \left( \frac{\sigma_{v2}}{\sqrt{n_2}} \right)^2, \quad (6)$$

the subscripts 1 and 2 denote two different sides of the rotation axis,  $\sigma_v$  and  $n$  are dispersion of the line-of-sight velocity and number of galaxies, respectively. According to MP17, a robust rotation detection requires satisfying three criteria simultaneously: (1) The ideal rotation

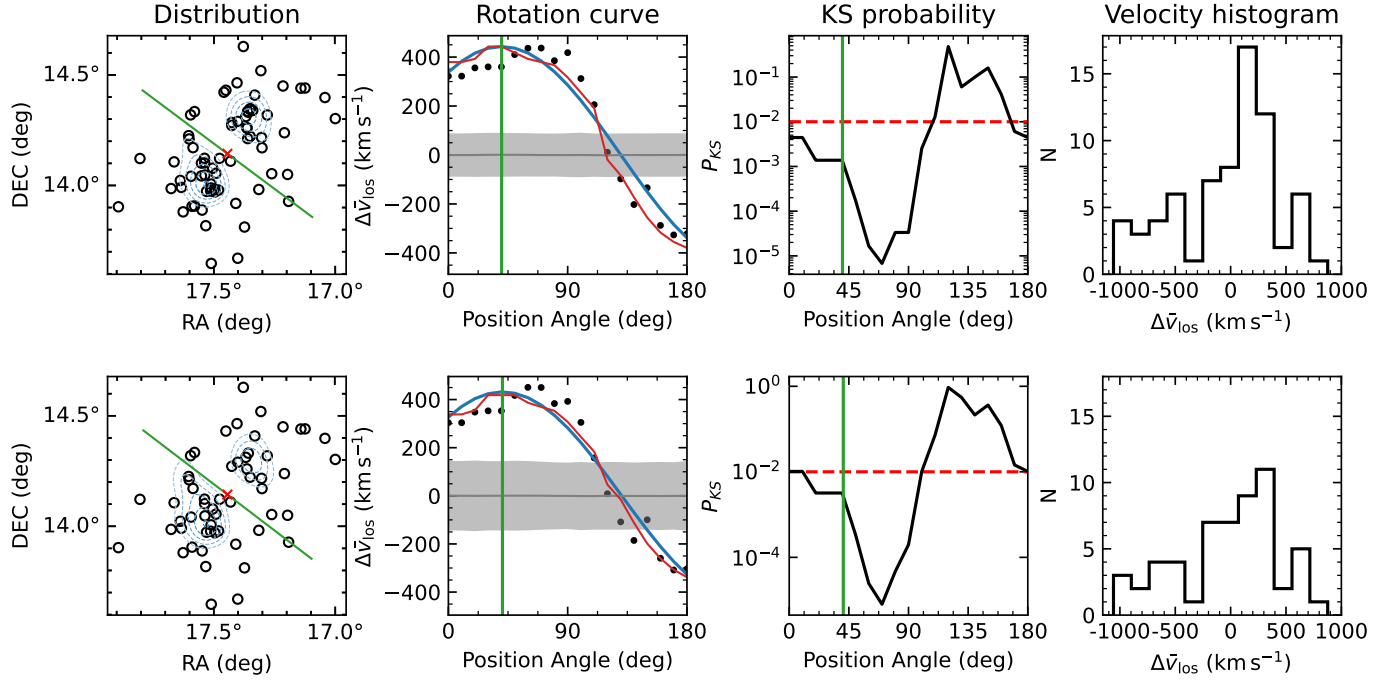


**Figure 3.** MP17 rotation analysis results for Case 1 (top row; all 71 members) and Case 2 (bottom row; 56 spectroscopic members). *Left:* Member galaxy distribution (black circle) with the best-fit rotation axis (green solid line). *Second column:* Rotation curves ( $\Delta\bar{v}_{\text{los}}$ ). Black dots: observed data; Blue curve: best-fit sinusoidal model; Red curve: ideal rotation profile; Gray curve/shading: random realizations with  $1\sigma$  scatter. *Third column:* KS two-sample test  $p$ -values. The red dashed line indicates  $p = 0.01$ ; the green line marks the best-fit axis angle. *Right:* Histograms of line-of-sight velocities.

model provides a good fit to the data ( $\chi^2_{\text{id}}/\text{dof} \leq 1$ ); (2) The rotation signal is significantly distinguishable from random noise ( $\chi^2_{\text{id}}/\chi^2_{\text{rd}} < 0.2$ ); and (3) The velocity distributions of the two subsamples are statistically distinct ( $P_{\text{KS}} < 0.01$ ).

We applied the MP17 methodology to investigate the rotation signal of RXCJ0110.0+1358. We acknowledge that MP17 suggests excluding substructures to prevent false positives. However, the strong kinematic deviation detected by the  $\delta$ -test in our cluster is not localized but spans the entire system. Excluding these high- $\delta$  members would effectively remove the primary signal of interest. Therefore, we apply the rotation analysis to the full sample to test whether this global kinematic structure aligns with an ordered rotation model.

Given the significant kinematic substructure signals detected in Sect. 3.1 (and the large offset of the BCG), we adopted the luminosity-weighted center as the reference center for rotation, since a rotation signal is often expected to be symmetric around the center of mass of the entire system. Figure 3 illustrates the results for both cases. The differential velocity curve,  $\Delta\bar{v}_{\text{los}}(\theta)$ , exhibits a sinusoidal variation with a maximum amplitude of  $\sim 443$  ( $\sim 432$ )  $\text{km s}^{-1}$  at a position angle of 40.17 (40.79) degrees. For the rotational scenario, we obtain a reduced chi-square of  $\chi^2_{\text{id}}/\text{dof} = 0.230(0.179)$ , satisfying

the first criterion. the derived rotation signal shows significant differences from the random expectation. The calculated ratio is  $\chi^2_{\text{id}}/\chi^2_{\text{rd}} = 0.026(0.027)$ , which falls well below the detection threshold of 0.2. Finally, we performed a two-sample Kolmogorov-Smirnov (KS) test to compare the velocity distributions of the galaxy subsamples on either side of the rotation axis. This test yields a  $p$ -value of  $P_{\text{KS}} \approx 1 \times 10^{-3}(3 \times 10^{-3})$ , which satisfies the significance threshold of  $P_{\text{KS}} < 0.01$ .

However, we note that the best-fit rotation axis effectively separates the southeastern main cluster from the northwestern substructure identified in Sect. 3.1. While such a configuration could theoretically arise from a merger of two clusters orbiting a common center of mass, the absence of corresponding substructures in both the X-ray emission and the weak lensing mass map renders this dynamical scenario unlikely (see Sect. 2.1 and Sect. 5.1). Instead, this alignment suggests that the signal is not due to coherent rotation, but rather originates from contamination by spatially distinct substructures (e.g., filaments or a small group of galaxies) projected along the line-of-sight.

The northwestern and southeastern components, as separated by the best-fit rotation axis, also exhibit distinct properties in their galaxy populations and kinematics. Figure 4 presents the color-magnitude diagram

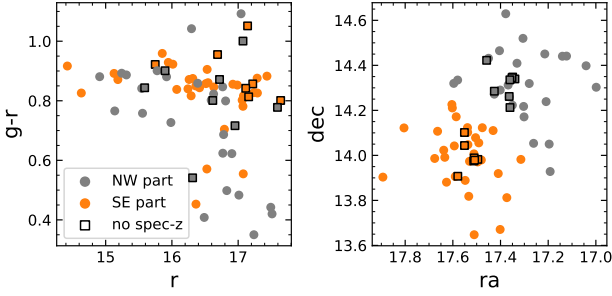


**Figure 4.** Properties of the member galaxies. *Left panel*: Magnitude - Color diagram. *Right panel*: Spatial distribution. In both panels, members associated with the northwestern and southeastern components are shown in orange and gray, respectively. Black hollow squares denote galaxies with redshifts estimated using the nearest-neighbor method.

using SDSS photometry, showing that while most member galaxies lie on the red sequence, a distinct population of blue galaxies is concentrated primarily within the northwestern component. Furthermore, treating the two components as spatially distinct groups reveals significant kinematic differences. The northwestern substructure is kinematically colder, with a velocity dispersion of  $\sigma_{\text{NW}} = 326$  (331)  $\text{km s}^{-1}$ , compared to the hotter southeastern component, with  $\sigma_{\text{SE}} = 548$  (548)  $\text{km s}^{-1}$ .

#### 4. SHAPE MEASUREMENT

##### 4.1. Basic Weak-lensing Theory

The deflection angle of light from background sources depends on the mass of the lens and the distances between the observer, lens, and background sources, which gives gravitational lensing the ability to infer the mass distribution of astrophysical objects. Weak lensing is widely used in studies of galaxy clusters; see [Umetsu \(2020\)](#) and [Meneghetti \(2021\)](#) for reviews.

Weak lensing can be measured through the distortion of images, which can be described with the Jacobian matrix  $\mathbf{A}$ :

$$\mathbf{A} = \begin{pmatrix} 1 - \kappa - \gamma_1 & -\gamma_2 \\ -\gamma_2 & 1 - \kappa + \gamma_1 \end{pmatrix}, \quad (7)$$

where  $\gamma_1$  and  $\gamma_2$  are the two components of shear, which stretch the image along two axes with an angle of  $45^\circ$ , while  $\kappa$  is the convergence, which describes its isotropic magnification. The convergence  $\kappa$  is related to the projected mass overdensity  $\Sigma(\theta)$ , which can be expressed as

$$\kappa(\theta) = \frac{\Sigma(\theta)}{\Sigma_{\text{cr}}}. \quad (8)$$

The critical surface density  $\Sigma_{\text{cr}}$  is in the form of

$$\Sigma_{\text{cr}} = \frac{c^2}{4\pi G} \frac{D_s}{D_l D_{ls}}, \quad (9)$$

where  $c$  and  $G$  are the speed of light and gravitational constant,  $D_s$ ,  $D_l$  and  $D_{ls}$  are the angular diameter distance between source and observer, lens and observer, lens and source, respectively. In practice, in the absence of information on the intrinsic size or magnitude of source galaxies, we can only observe the reduced shear  $g = \gamma/(1 - \kappa)$ .

In the weak lensing regime, the observed ellipticity  $e_{\text{obs}}$  is the complex sum of the intrinsic ellipticity of a source  $e_s$  and the reduced shear  $g$  from lensing. The reduced shear of a single galaxy is much smaller than its intrinsic ellipticity, which makes it difficult to measure for an individual galaxy. We can assume that the intrinsic ellipticities are randomly distributed, therefore their expectation value is  $\langle e_s \rangle = 0$ . By stacking a large number of galaxies, the reduced shear can be estimated from the averaged observed ellipticities.

##### 4.2. PSF Star Selection

Astronomical images suffer from the point spread function (PSF) caused by the optical system and the atmosphere if the telescope is ground-based (see [Liaudat et al. 2023](#) for a review). An uncorrected PSF will bias shape measurements, a critical issue given that weak lensing distortions are typically at the one-percent level. The modeling and correction of the PSF is a crucial step before shape measurement.

Stars are ideal objects for PSF modeling, since they are natural point sources and are not distorted by the lensing effect. The PSF varies over time; therefore, PSF stars should be extracted on single-exposure images. We first run SExtractor for single exposure images, removing the artifacts by setting the DETECT\_MINAREA = 10, which corresponds to a radius of  $\sim 2$  pixels. A pre-selection of  $\text{FLAGS} \leq 4$  is applied to the catalog of each exposure to exclude sources with bad results. The saturated stars are then removed according to the distribution of MU\_MAX. PSF star candidates are then selected from the stellar locus in the MU\_MAX - MAG\_AUTO diagram, where unsaturated stars form a tight, well-defined sequence.

We applied a magnitude cut of 22.5 to exclude those objects that might be contamination from galaxies. Finally, we select those stars with  $\text{FLAGS} == 0$  to exclude sources with bad pixels or blended with other objects. For each exposure, about 2,500 PSF stars are selected for PSF modeling.

##### 4.3. Lensfit PSF Modeling and Shape Measurement

[lensfit](#) ([Miller et al. 2013](#)) was first used in CFHTLenS ([Heymans et al. 2012](#)) for shape measurement, and it proved to be a powerful tool for weak-lensing analysis. Given that our data were also taken

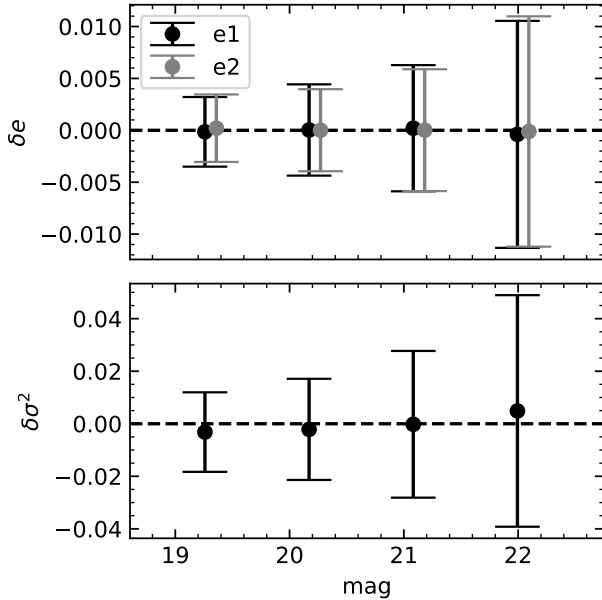


**Figure 5.** Residuals of ellipticity and size between PSF model and PSF star.

with the CFHT MegaCam, we adopt the well-tested `lensfit` pipeline for both PSF modeling and shape measurement.

`lensfit` models the PSF on a pixel grid. To account for spatial variations across the field of view, the value of each pixel in this model is described by a polynomial function of the position on the detector mosaic. Following Fu et al. (2018), we configure this built-in model by setting its key parameters: the polynomial order for the global, field-of-view variation is set to four, while the order for chip-dependent variations on individual CCDs is set to one. Figure 5 shows the fitted PSF model and the residual between the PSF model and stars of 4 exposures. The average ellipticity before correction is  $\langle e_1 \rangle = 2.17 \times 10^{-3}$  and  $\langle e_2 \rangle = 1.86 \times 10^{-3}$ , after correction, the mean residual ellipticities are reduced to  $\langle e_1 \rangle = -4.71 \times 10^{-4}$  and  $\langle e_2 \rangle = 1.17 \times 10^{-5}$ , showing a significant decrease, as expected.

After PSF modeling, shear measurements are carried out with a likelihood-based method, the ellipticity is then given by fitting the galaxy postage stamps with a PSF convolved two-component (bulge + disk) model. The detailed algorithm of `lensfit` are described in Miller et al. 2007, Kitching et al. 2008 and Miller et al. 2013.

#### 4.4. Source Selection

The galaxy cluster has a low redshift of 0.05828, according to the photo- $z$  catalog from CFHTLS (Hildebrandt et al. 2012), only 1.21% of galaxies have  $z_{\text{phot}} <$

0.058, which means that the lensing signal is dominated by the background sources. Furthermore, with photometric data in only four bands, the resulting photo- $z$  accuracy is insufficient to reliably separate foreground member galaxies from the background source population. Therefore, we only applied a magnitude cut of  $21 < m_r < 26$  on the selection of background sources.

In addition to the magnitude cut, `lensfit` has a strict selection of background sources before and during the fitting process. Objects that are too large for the postage stamp, are heavily blended, or fail the model-fitting procedure are assigned a weight of zero and are thus excluded from the final shear catalog. For the other galaxies, a weight and flag are assigned, the weight is based on shape noise and ellipticity-measurement noise. To further increase the reliability, we select the galaxies observed in 4 exposures. Additionally, we applied a size cut of the final shear catalog, excluding galaxies with  $r_{ab} < 0.3 r_{\text{PSF}}$ , where  $r_{ab}$  indicates the geometric mean of the major and minor-axis scalelength, and  $r_{\text{PSF}}$  is the  $r_{ab}$  of PSF model at the position of galaxy. The final catalog contains 53,006 source galaxies, corresponding to a number density of approximately 15 galaxies arcmin $^{-2}$ .

#### 4.5. Shear Calibration

The measured shear can be biased by a variety of instrumental and astrophysical effects (Meneghetti 2021). Generally, the observed reduced shear,  $g^{\text{obs}}$ , is modeled as being linearly biased with respect to the true shear,  $g^{\text{true}}$ , by a multiplicative coefficient,  $m_i$ , and an additive coefficient,  $c_i$ .

$$g_i^{\text{obs}} = (1 + m_i)g_i^{\text{true}} + c_i. \quad (10)$$

Following Liu et al. (2018), shear calibration is carried out with image simulation based on `Galsim` (Rowe et al. 2015). The mock galaxy catalogs are generated with the same coordinates and magnitude as the observed data, which ensures the distribution of galaxies in a more realistic way. Galaxies are generated with the same two components used in Miller et al. (2013), with a bulge-to-total flux ratio ( $B/T$ ) which is a truncated Gaussian distribution with  $\mu = 0.0$  and  $\sigma = 0.1$ . 10% of galaxies are set as bulge-dominant galaxies with  $B/T = 1.0$ . The Sérsic index distribution of disk galaxies is truncated Gaussian with  $\mu = 0.72$  and  $\sigma = \sqrt{0.15}$ , ranging from 0.3-4.0, where indices exceeding 4.0 are set to 4.0. For bulge-dominated galaxies, the Sérsic index is set to 4.0. The scale length radius follows the distribution given in Kuijken et al. (2015),

$$\log_e(r_d) = -1.320 - 0.278(r - 23). \quad (11)$$

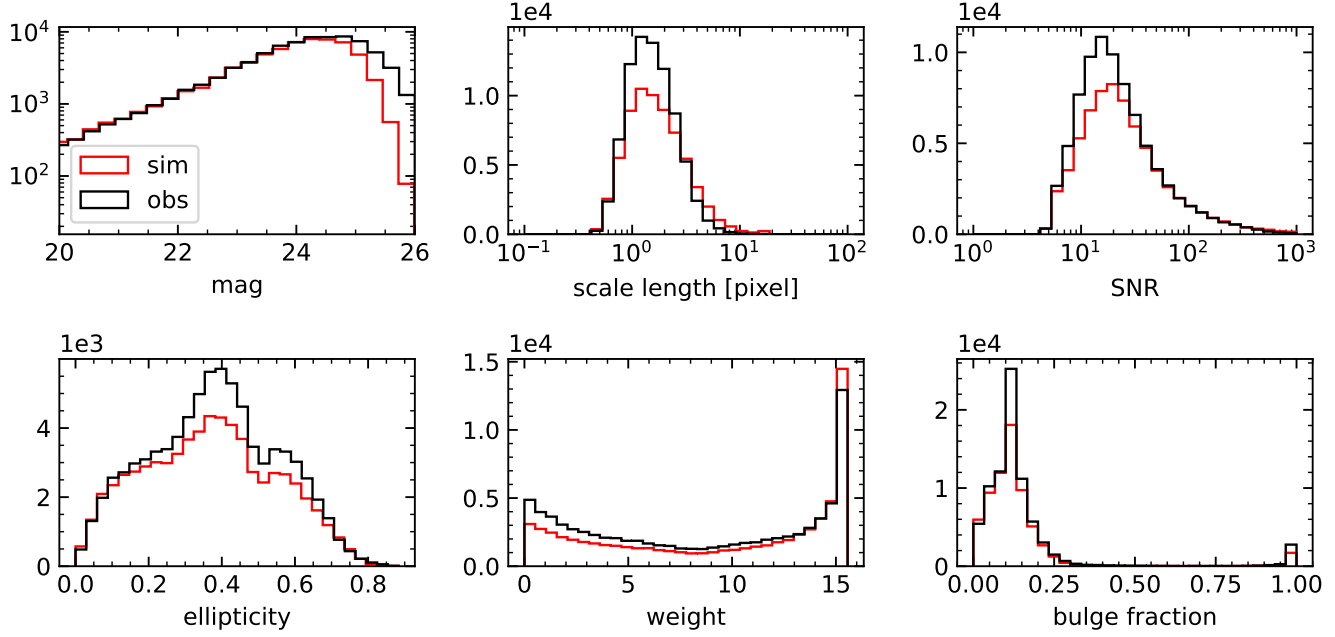


**Figure 6.** Comparison of observed data (black) and mock data (red) for distributions of galaxy properties. From left to right, top to bottom: magnitude, scale length, signal to noise ratio, ellipticity, lensfit weights and bulge fraction.

The intrinsic ellipticity of disk galaxies follows the distribution given in [Miller et al. \(2013\)](#)

$$p(e) = \frac{Ae(1 - \exp(e - e_{\max})/a)}{(1 + e)(e^2 + e_0^2)^{1/2}}, (e < e_{\max}), \quad (12)$$

where we adopted  $a = 0.2539$ ,  $e_{\max} = 0.803$  and  $e_0 = 0.0256$  from [Miller et al. \(2013\)](#). For bulge-dominated galaxies, the distribution of ellipticity is

$$p(e) \propto e \exp(-be - ce^2), \quad (13)$$

with  $b = 2.368$  and  $c = 6.691$ .

We applied the same WCS information from the header of the observations on the mock images to reproduce the dithering pattern of the observation. The mock images are then generated on the basis of the mock galaxy catalog. We apply a constant shear modulus of  $|\gamma| = 0.04$  along four directions,  $(+0.0283, +0.0283)$ ,  $(-0.0283, -0.0283)$ ,  $(-0.0370, +0.0153)$  and  $(+0.0153, 0.0370)$ . To suppress shape noise, we employ the shape-pair cancellation technique by rotating the galaxy images by  $90^\circ$ . The total number of mock galaxies is  $\sim 1.4 \times 10^6$ .

For each set of images, we applied the same PSF models fitted from the observation data. Noise is added according to sky noise, readout noise, and gain in headers. This noise, combined with random galaxy shapes, resulted in the non-detection of faint sources, reducing the final effective number of galaxies. Figure 6 shows

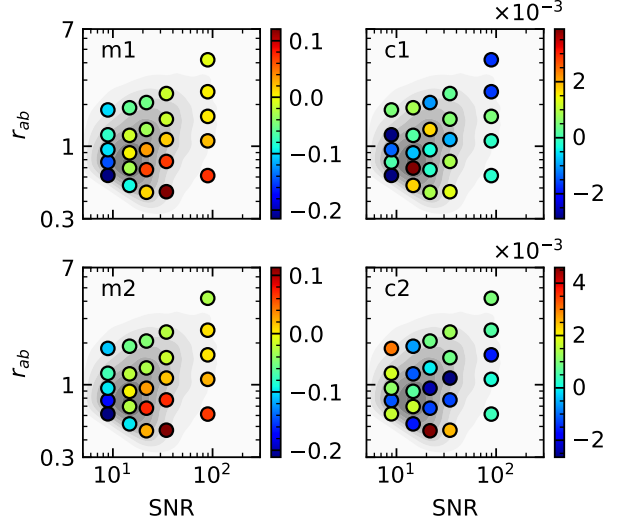


**Figure 7.** Shear bias coefficients on  $\text{SNR}-r_{ab}$  surface. *Right panels* are the multiplicative bias, *left panels* are the additive bias. Background filled contours indicate the number of galaxies.

the comparison of the mock and obs different parameters given by the `lensfit` for galaxies with weight  $> 0$ .

We followed [Liu et al. \(2018\)](#) and binned the galaxies on a  $\text{SNR}-r_{ab}$  surface, where  $r_{ab}$  is the geometric average of the major and minor axes in scale length. Considering that our mock sample size is relatively small, the

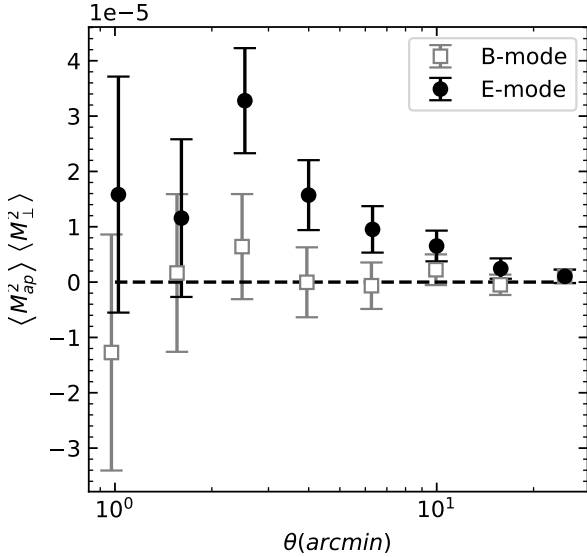


**Figure 8.** E-/ B-mode from aperture mass dispersion.

galaxies are binned into  $5 \times 5$  bins, such that the number of galaxies in each bin is identical. For each bin, we fitted the input shear and measured shear with Eq. 10 to get the additive and multiplicative bias coefficients, the results are shown in Figure 7. The shear of observed galaxies are then calibrated according to the bins they fall into.

#### 4.6. Systematic Tests

Weak lensing is in general sensitive to systematic errors. In an ideal case, the gravitational shear field is curl-free and purely constitutes an E-mode. Consequently, the presence of a divergence-free B-mode serves as a diagnostic for residual systematics. Before mass map construction and mass estimation, we performed an E- and B-mode separation test using the aperture mass dispersion from the shear two-point correlation function (2PCF). It is well established that observable B-modes mainly originate from imperfections in image processing and data-analysis pipelines (Kilbinger 2015), with intrinsic galaxy alignments producing subdominant contributions on small scales. Figure 8 presents the measured results of the E / B mode decomposition. The B-mode is close to 0 at all scales, while a significant E-mode is observed at  $2'$  to  $10'$ .

## 5. RESULTS AND DISCUSSION

### 5.1. Mass Reconstruction and Estimation

Using the shear catalog described in Section 4.4, we performed mass reconstruction using two methods. For the standard Fourier inversion method (Kaiser & Squires

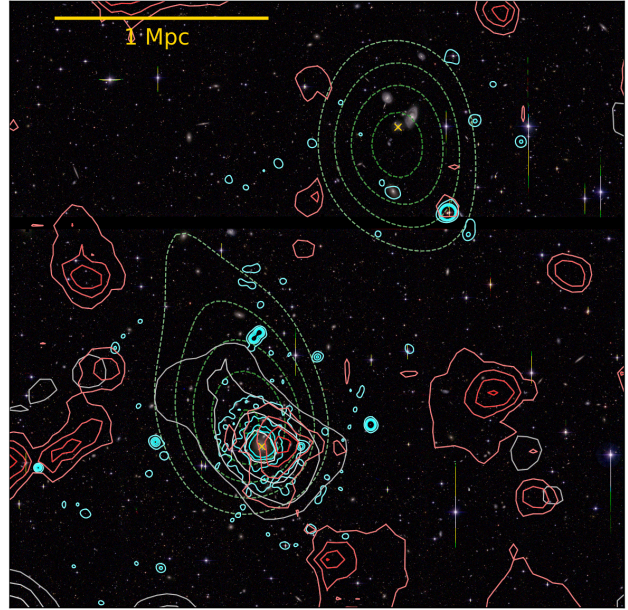


**Figure 9.** Reconstructed 2D mass map is shown in white contours, ranging from  $1.2\sigma$  to  $2.64\sigma$ . X-ray emission from XMM-Newton is illustrated with cyan contours, ranging from  $5\sigma$  to  $25\sigma$ . The green dashed contours indicate the luminosity map. The background shows the rgb image coadded from the  $i$ ,  $r$  and  $g$  bands. The BCG and the brightest galaxy of the northwest region are marked with yellow crosses. Red contours are the results given by `Glimpse` with  $\lambda = 3.5$

1993, hereafter KS93), we binned the shear map into a  $90 \times 90$  pixel grid. The shear can be transformed into E- and B-mode convergence fields  $\kappa_E$  and  $\kappa_B$ , respectively, as:

$$\tilde{\kappa}_E = (k_1^2 - k_2^2)\tilde{\gamma}_1 + 2k_1k_2\tilde{\gamma}_2/(k_1^2 + k_2^2), \quad (14)$$

and

$$\tilde{\kappa}_B = (k_1^2 - k_2^2)\tilde{\gamma}_1 - 2k_1k_2\tilde{\gamma}_2/(k_1^2 + k_2^2), \quad (15)$$

where the tildes denote Fourier transforms, and  $k$  is the wave number. The obtained convergence map was then smoothed using an aperture mass filter from Schneider et al. (1998) with a radius of  $13.3'$  (20 pixels) to obtain the final mass map. In addition, we applied `Glimpse` (Lanusse et al. 2016), which employs sparse regularization in the wavelet domain to recover convergence fields directly from irregularly sampled data without the need for prior binning.

Figure 9 presents the reconstructed mass maps. The KS93 results show that the mass is predominantly concentrated in the southeast, coincident with the BCG position and consistent with the X-ray surface brightness. Notably, no significant over-density is visually

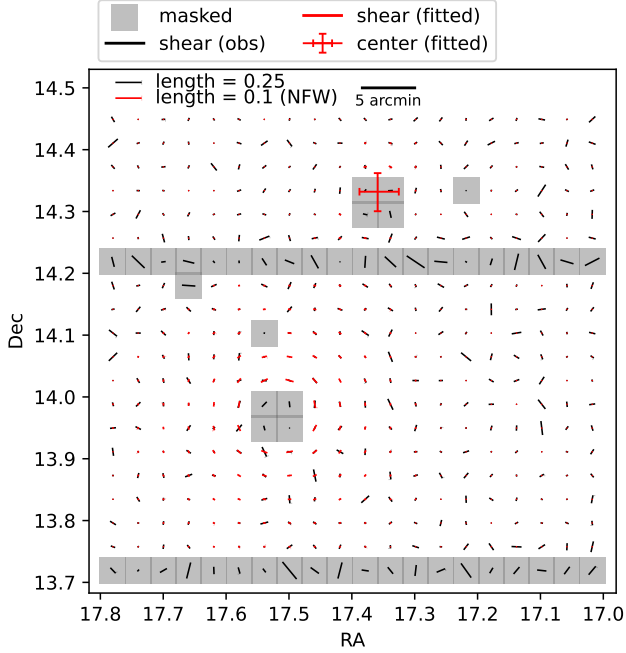


**Figure 10.** 2D shear vector map. The black segments represent the binned observed shear, while the red segments show the best-fit model shear derived from the linear superposition of two NFW profiles. Grey regions indicate pixels masked due to low source galaxy density ( $n_{\text{gal}} < 50$ ). The red cross marks the best-fit position of the northwestern (NW) component with  $1\sigma$  uncertainty.

detected in the northwestern region corresponding to the secondary optical peak. Additionally, although the `Glimpse` result is noisy, the mass distribution near BCG and NW optical peak is in agreement with KS93.

To quantitatively assess the contribution of the northwestern substructure, we performed a parametric 2D shear fitting analysis assuming a dual-halo model. The source redshift distribution is estimated using a subset of the COSMOS catalog (Shuntov et al. 2025). Since CFHT  $r$ -band is not available in this catalog, we adopted the HSC  $r$ -band magnitude as a proxy. We selected a reference sample by applying the same magnitude cuts  $21 < m_{r,\text{HSC}} < 26$  and a size cut of half-light radius  $> 0.5$  arcsec. While this size cut is stricter than the one applied to the shear catalog, it ensures that the reference redshift distribution is derived from well-resolved sources with reliable photometric redshifts, serving as a robust proxy for the lensing source population dominated by `lensfit`-weighted galaxies.

As Figure 10 shows, we selected a  $0.8^\circ \times 0.8^\circ$  sub-field centered on the luminosity-weighted centroid of the system and binned the shear data into a  $20 \times 20$  grid to reduce shape noise. The mass distribution was modeled as the sum of two Navarro-Frenk-White (NFW) profiles

(Navarro et al. 1997) halos at  $z_{\text{cl}} = 0.05828$ . The main halo was fixed at the BCG position, while the northwestern halo was initialized at the position of its brightest galaxy (ra = 17.358, dec = 14.332 deg) and allowed to vary.

Following Du et al. (2015), the model shear at each pixel is the linear superposition of the shear fields generated by the two NFW profiles. To mitigate the degeneracy between mass and concentration given the limited signal-to-noise ratio, we did not fit the concentration as a free parameter. Instead, the concentration  $c_{200}$  was directly determined from the mass  $M_{200}$  using the mass-concentration relation of Xu et al. (2021). Consequently, only the masses of the two halos (and the position of the northwestern halo) were treated as free parameters. To ensure stability, we masked pixels containing fewer than 50 source galaxies, as well as the central  $2 \times 2$  pixels of each NFW halo.

The fitting is performed with mass bounds of  $12.5 < \log M_{200} < 15.5$ , and a positional constraint of  $0.1$  deg in both  $\Delta\text{RA}$  and  $\Delta\text{Dec}$ . Parameter estimation was performed in two steps. We first utilized the Differential Evolution algorithm with Latin Hypercube Sampling to locate the global maximum likelihood solution, mitigating the risk of local minima. This solution was then used to initialize the MCMC walkers. This 2D analysis yields a best-fit mass of  $\log(M_{200}/M_{\odot}) = 13.98^{+0.30}_{-0.50}$  for the southeastern main cluster and  $\log(M_{200}/M_{\odot}) = 13.07^{+0.50}_{-0.39}$  for the northwestern component. This mass ratio is remarkably consistent with the dynamical estimates derived from the velocity dispersions ( $\sigma_{\text{SE}} \approx 548$  km s $^{-1}$  and  $\sigma_{\text{NW}} \approx 326$  km s $^{-1}$ ), which predict a secondary mass of  $\log M \approx 13.3$  assuming the scaling relation  $M \propto \sigma_v^3$ . This result suggests that while a low-mass group may exist in the northwest, its mass is approximately an order of magnitude lower than that of the main cluster, explaining its non-detection in the visual mass maps.

Given the dominance of the main halo, we proceed to characterize the cluster properties using a 1D azimuthally averaged tangential shear profile centered on the BCG. We decomposed the shear components into tangential ( $\gamma_t$ ) and cross ( $\gamma_x$ ) components:

$$\gamma_t = -\gamma_1 \cos(2\Phi) - \gamma_2 \sin(2\Phi), \quad (16)$$

and

$$\gamma_x = -\gamma_1 \sin(2\Phi) + \gamma_2 \cos(2\Phi) \quad (17)$$

where  $\Phi$  is the position angle with respect to the selected center.  $\gamma_x$  can provide a diagnostic test for systematic error, which should be zero for an ideal shear profile. We computed the azimuthally averaged shear profile by

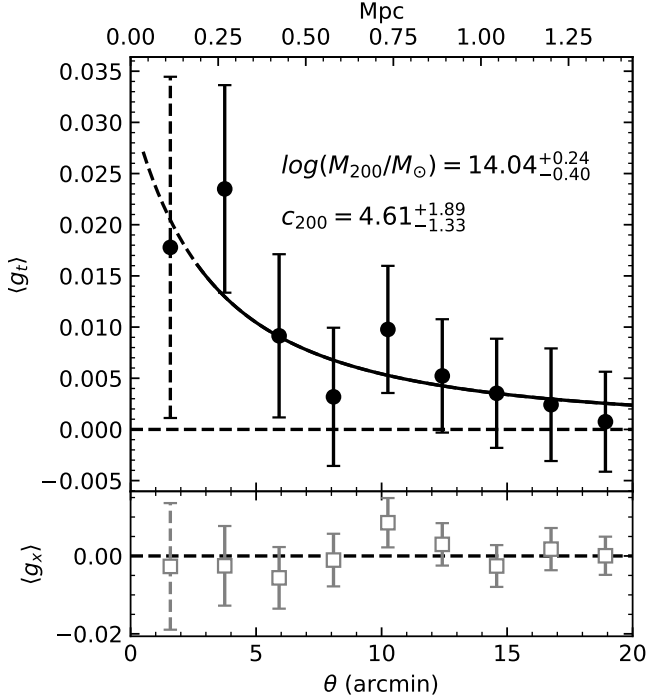


**Figure 11.** Radial dependence of the tangential (black dots) and cross components (grey hollow squares), the best-fit NFW profile is shown in black line. The inner region (0.5'-2.6'), indicated by the dashed curve and dashed error bars, was not included in the fit and is plotted for display only.

binning galaxies according to their projected radial distances from the cluster center. The bins range from 2.6 to 20 arcmin (corresponding to 0.2 -1.5 Mpc on the lens plane). The mean tangential shear within each bin is weighted by the `lensfit` weights.

The observed profile is modeled using a single NFW halo centered on the BCG. Parameter estimation is also performed with MCMC. In contrast to the 2D analysis, we incorporated the full source redshift distribution to improve accuracy. Instead of adopting a single mean redshift, we integrated over the redshift distribution of the selected COSMOS source sample to compute the theoretical shear for each bin. Furthermore, we treated the concentration parameter  $c_{200}$  as a free parameter. To mitigate degeneracy while allowing for intrinsic scatter, we employed the mass-concentration relation from Xu et al. (2021) as a prior (rather than a deterministic constraint). Our fitting results and the tangential shear profile are shown in Figure 11. This analysis yields a mass of  $\log(M_{200}/M_\odot) = 14.04^{+0.24}_{-0.40}$  and a concentration of  $c_{200} = 4.61^{+1.89}_{-1.33}$ .

## 5.2. Discussion

Our multi-wavelength analysis reveals inconsistency between X-ray and optical observations of RXCJ0110.0+1358. While the optical luminosity map displays a distinct bimodal structure with dual luminosity centers in the southeast and northwest regions, the X-ray emission shows an ICM detection only in the southeastern component. This absence of X-ray counterparts in the northwestern region suggests two possible interpretations: either the apparent substructure lacks genuine physical association or we are witnessing a merger in its early stages.

The distinct properties of the northwestern galaxies provide crucial clues to their origin. As shown in Figure 4, their bluer colors and significantly lower velocity dispersion are characteristic of a star-forming galaxy population within a filamentary structure, rather than a virialized component of the main cluster.

Our weak lensing analysis provides critical insights into this inconsistency. The reconstructed mass map shows strong alignment between the primary mass overdensity and the X-ray emission centroid in the southeastern region. In contrast, no massive structure is detected near the northwest luminosity center. Our parametric dual-halo fitting further constrains the mass of this northwestern component to  $\log(M_{200}/M_\odot) = 13.07$ , an order of magnitude lower than the main cluster. This explains its non-detection in the non-parametric mass map and confirms that it acts merely as a perturbation rather than a major merger component. This immense mass disparity also rules out the possibility that the northwestern component is dynamically capable of driving a global rotation of the system.

By fitting a single NFW profile to the tangential shear signal of the main cluster, we measure a mass of  $\log(M_{200}/M_\odot) = 14.04^{+0.24}_{-0.40}$ . Comparing this result with other estimators reveals an instructive picture. This value, though lower than previous estimates of Y12, statistically consistent with predictions from the  $M_{200} - T_X$  relation ( $\log M_{200} = 14.33$ ) within the measurement uncertainties (difference  $\lesssim 1.3\sigma$ ). The  $\sim 0.3$  dex offset is well within the typical intrinsic scatter observed in cluster mass scaling relations, particularly for low-to-moderate mass systems where shape noise is significant.

Based on the estimated weak lensing mass, we find  $r_{200} \approx 1$  Mpc (corresponding to  $14'$  at  $z = 0.058$ ), while the northwestern optical structure lies  $22'$  ( $\sim 1.6 r_{200}$ ) away from the BCG. In view of this spatial separation, combined with the absence of associated mass or X-ray emission, and the difference in colors, we consider two potential scenarios. One possibility is a low-mass galaxy group in an early stage of infall. Indeed, given the sen-

sitivity limits of our weak lensing map, such a low-mass system could arguably evade detection. However, the distinct properties of the galaxy population favor the alternative scenario: that the northwestern component is a chance projection of filament. This filament hypothesis is consistent with the full range of our observations: 1) the lack of a significant mass concentration from weak lensing; 2) the absence of detectable ICM in X-rays; and 3) the presence of a kinematically colder, bluer galaxy population. The known high false-positive rates (25%–40%) of optical group-finders (Koester et al. 2007; Starikova et al. 2014) can readily explain the misclassification of these filament galaxies as cluster members, which in turn generated the spurious rotation signal and substructure claims.

## 6. SUMMARY

The galaxy cluster RXCJ0110.0+1358, a candidate rotating system, displays a bimodal luminosity structure with dual peaks in the southeast and northwest. Using the MP17 method to probe rotational signatures and the  $\delta$ -test to identify substructures, we demonstrate that the apparent rotation signal is spurious, originating entirely from the northwest substructure rather than a coherent rotation of the cluster. Furthermore, significant discrepancies emerge between the X-ray and optical views: specifically, while the optical data show a prominent northwestern component, the X-ray emission reveals no corresponding extended structure.

We then conducted a weak lensing analysis using new deep  $r$ -band imaging from CFHT MegaCam. The reconstructed mass map aligns well with the X-ray morphology, showing a mass concentration coincident with the BCG located at southeastern luminosity peak and ICM distribution. No significant mass overdensity is observed near the northwestern luminosity center.

Mass estimates reveal a notable discrepancy with previous catalog values. While Y12 reported a mass of  $\log(M_{200}/M_{\odot}) = 14.43$ , our weak lensing analysis yields a mass of  $\log(M_{200}/M_{\odot}) = 14.04^{+0.24}_{-0.40}$  for the main cluster. We attribute this difference primarily to the projection of the filamentary structure, which leads to an overestimation of richness in optical catalogs, combined

with the large intrinsic scatter inherent to mass measurements of low-mass clusters..

These results demonstrate that the apparent northwestern substructure and its associated rotation signal are not intrinsic to the cluster. The convergence of our weak lensing mass map and the X-ray ICM emission firmly establishes the southeastern component as the sole gravitational center. Crucially, our dual-halo fitting limits the northwestern mass to  $\sim 10^{13} M_{\odot}$ —an order of magnitude lower than the main cluster—ruling out the possibility that it is dynamically capable of driving the observed global rotation. The northwestern optical peak, therefore, is best explained as a chance projection of a filament, given its lack of hot gas and its kinematically colder, bluer galaxy population. The misclassification of these filament galaxies as cluster members by the optical group-finding algorithm fully accounts for the spurious rotation signal, the optically-identified substructure, and the previous overestimation of the total cluster mass.

L.P. F. acknowledges the supports from NSFC No. 12541302, the Innovation Program of Shanghai Municipal Education Commission (Grant No. 2025GDZKZD04), and China Manned Space Project with Grant No. CMS-CSST-2025-A05. W.D. acknowledges the support from the NSFC under grant No. 12541302 and the China Manned Spaced (CMS) program with grant Nos. CMS-CSST-2025-A02, and CMS-CSST-2025-A03. R. W. and D. T. were supported by a NASA/ADAP grant to Michigan State University (NASA-80NSSC22K0476). W.L. and B.L. acknowledge the support from the National Key Research and Development Program of China (2023YFA1608100). B.L. acknowledges the Double-Innovation Doctor Program of Jiangsu Province (No. JSSCBS0216).

*Facilities:* CFHT (MegaCam)

*Software:* cedproc (Craig et al. 2017), EAZY (Brammer et al. 2008), lensfit (Miller et al. 2013), photutils (Bradley et al. 2024), SAS (Gabriel et al. 2004), SCAMP (Bertin 2006), Source Extractor (Bertin & Arnouts 1996), SWarp (Bertin 2010), XSPEC (Arnaud 1996)

## REFERENCES

Abazajian, K. N., Adelman-McCarthy, J. K., Agüeros, M. A., et al. 2009, ApJS, 182, 543, doi: [10.1088/0067-0049/182/2/543](https://doi.org/10.1088/0067-0049/182/2/543)

Allen, S. W., Evrard, A. E., & Mantz, A. B. 2011, ARA&A, 49, 409, doi: [10.1146/annurev-astro-081710-102514](https://doi.org/10.1146/annurev-astro-081710-102514)

Altamura, E., Kay, S. T., Chluba, J., & Towler, I. 2023, Monthly Notices of the Royal Astronomical Society, 524, 2262, doi: [10.1093/mnras/stad1841](https://doi.org/10.1093/mnras/stad1841)

Arnaud, K. A. 1996, in Astronomical Society of the Pacific Conference Series, Vol. 101, Astronomical Data Analysis Software and Systems V, ed. G. H. Jacoby & J. Barnes, 17

Arnold, T. J., Martini, P., Mulchaey, J. S., Berti, A., & Jeltema, T. E. 2009, ApJ, 707, 1691, doi: [10.1088/0004-637X/707/2/1691](https://doi.org/10.1088/0004-637X/707/2/1691)

Baldi, A. S., De Petris, M., Sembolini, F., et al. 2018, MNRAS, 479, 4028, doi: [10.1093/mnras/sty1722](https://doi.org/10.1093/mnras/sty1722)

Bertin, E. 2006, in Astronomical Society of the Pacific Conference Series, Vol. 351, Astronomical Data Analysis Software and Systems XV, ed. C. Gabriel, C. Arviset, D. Ponz, & S. Enrique, 112

Bertin, E. 2010, SWarp: Resampling and Co-adding FITS Images Together, Astrophysics Source Code Library, record ascl:1010.068

Bertin, E., & Arnouts, S. 1996, A&AS, 117, 393, doi: [10.1051/aas:1996164](https://doi.org/10.1051/aas:1996164)

Bilton, L. E., Hunt, M., Pimbblet, K. A., & Roediger, E. 2019, Monthly Notices of the Royal Astronomical Society, 490, 5017, doi: [10.1093/mnras/stz2927](https://doi.org/10.1093/mnras/stz2927)

Bleem, L. E., Stalder, B., de Haan, T., et al. 2015, ApJS, 216, 27, doi: [10.1088/0067-0049/216/2/27](https://doi.org/10.1088/0067-0049/216/2/27)

Boulade, O., Charlot, X., Abbon, P., et al. 2003, in Society of Photo-Optical Instrumentation Engineers (SPIE) Conference Series, Vol. 4841, Instrument Design and Performance for Optical/Infrared Ground-based Telescopes, ed. M. Iye & A. F. M. Moorwood, 72–81, doi: [10.1117/12.459890](https://doi.org/10.1117/12.459890)

Bradley, L., Sipőcz, B., Robitaille, T., et al. 2024, astropy/photutils: 2.0.2, 2.0.2, Zenodo, doi: [10.5281/zenodo.13989456](https://doi.org/10.5281/zenodo.13989456)

Brammer, G. B., van Dokkum, P. G., & Coppi, P. 2008, The Astrophysical Journal, 686, 1503, doi: [10.1086/591786](https://doi.org/10.1086/591786)

Chluba, J., & Mannheim, K. 2002, A&A, 396, 419, doi: [10.1051/0004-6361:20021429](https://doi.org/10.1051/0004-6361:20021429)

Cooray, A., & Chen, X. 2002, ApJ, 573, 43, doi: [10.1086/340582](https://doi.org/10.1086/340582)

Craig, M., Crawford, S., Seifert, M., et al. 2017, astropy/ccdproc: v1.3.0.post1, doi: [10.5281/zenodo.1069648](https://doi.org/10.5281/zenodo.1069648)

Danese, L., de Zotti, G., & di Tullio, G. 1980, A&A, 82, 322

Dressler, A., & Shectman, S. A. 1988, AJ, 95, 985, doi: [10.1086/114694](https://doi.org/10.1086/114694)

Du, W., Fan, Z., Shan, H., et al. 2015, ApJ, 814, 120, doi: [10.1088/0004-637X/814/2/120](https://doi.org/10.1088/0004-637X/814/2/120)

Ettori, S., Donnarumma, A., Pointecouteau, E., et al. 2013, SSRv, 177, 119, doi: [10.1007/s11214-013-9976-7](https://doi.org/10.1007/s11214-013-9976-7)

Fu, L., Liu, D., Radovich, M., et al. 2018, Monthly Notices of the Royal Astronomical Society, 479, 3858, doi: [10.1093/mnras/sty1579](https://doi.org/10.1093/mnras/sty1579)

Gabriel, C., Denby, M., Fyfe, D. J., et al. 2004, in Astronomical Society of the Pacific Conference Series, Vol. 314, Astronomical Data Analysis Software and Systems (ADASS) XIII, ed. F. Ochsenbein, M. G. Allen, & D. Egret, 759

Gaia Collaboration, Brown, A. G. A., Vallenari, A., et al. 2018, A&A, 616, A1, doi: [10.1051/0004-6361/201833051](https://doi.org/10.1051/0004-6361/201833051)

Gu, L., Xu, H., Gu, J., et al. 2012, ApJ, 749, 186, doi: [10.1088/0004-637X/749/2/186](https://doi.org/10.1088/0004-637X/749/2/186)

Heisler, J., Tremaine, S., & Bahcall, J. N. 1985, ApJ, 298, 8, doi: [10.1086/163584](https://doi.org/10.1086/163584)

Heymans, C., Van Waerbeke, L., Miller, L., et al. 2012, Monthly Notices of the Royal Astronomical Society, 427, 146, doi: [10.1111/j.1365-2966.2012.21952.x](https://doi.org/10.1111/j.1365-2966.2012.21952.x)

Hildebrandt, H., Erben, T., Kuijken, K., et al. 2012, MNRAS, 421, 2355, doi: [10.1111/j.1365-2966.2012.20468.x](https://doi.org/10.1111/j.1365-2966.2012.20468.x)

Hwang, H. S., & Lee, M. G. 2007, The Astrophysical Journal, 662, 236, doi: [10.1086/514328](https://doi.org/10.1086/514328)

Kaiser, N., & Squires, G. 1993, ApJ, 404, 441, doi: [10.1086/172297](https://doi.org/10.1086/172297)

Kang, W., Hwang, H. S., Song, H., et al. 2024, A Deep Redshift Survey of the Perseus Cluster: Spatial Distribution and Kinematics of Galaxies, arXiv. <http://arxiv.org/abs/2403.19307>

Kilbinger, M. 2015, Reports on Progress in Physics, 78, 086901, doi: [10.1088/0034-4885/78/8/086901](https://doi.org/10.1088/0034-4885/78/8/086901)

Kitching, T. D., Miller, L., Heymans, C. E., van Waerbeke, L., & Heavens, A. F. 2008, Monthly Notices of the Royal Astronomical Society, 390, 149, doi: [10.1111/j.1365-2966.2008.13628.x](https://doi.org/10.1111/j.1365-2966.2008.13628.x)

Kneib, J.-P., & Natarajan, P. 2011, A&A Rev., 19, 47, doi: [10.1007/s00159-011-0047-3](https://doi.org/10.1007/s00159-011-0047-3)

Koester, B. P., McKay, T. A., Annis, J., et al. 2007, ApJ, 660, 221, doi: [10.1086/512092](https://doi.org/10.1086/512092)

Kravtsov, A. V., & Borgani, S. 2012, ARA&A, 50, 353, doi: [10.1146/annurev-astro-081811-125502](https://doi.org/10.1146/annurev-astro-081811-125502)

Kuijken, K., Heymans, C., Hildebrandt, H., et al. 2015, MNRAS, 454, 3500, doi: [10.1093/mnras/stv2140](https://doi.org/10.1093/mnras/stv2140)

Lanusse, F., Starck, J.-L., Leonard, A., & Pires, S. 2016, A&A, 591, A2, doi: [10.1051/0004-6361/201628278](https://doi.org/10.1051/0004-6361/201628278)

Liaudat, T., Starck, J.-L., & Kilbinger, M. 2023, Frontiers in Astronomy and Space Sciences, 10, 1158213, doi: [10.3389/fspas.2023.1158213](https://doi.org/10.3389/fspas.2023.1158213)

Liu, B., Luo, W., Kilbinger, M., et al. 2025, submitted, CFHT MegaCam Two Deep Fields Imaging Survey (2DFIS) I: Overview

Liu, D., Fu, L., Liu, X., et al. 2018, MNRAS, 478, 2388, doi: [10.1093/mnras/sty1219](https://doi.org/10.1093/mnras/sty1219)

Manolopoulou, M., & Plionis, M. 2017, Monthly Notices of the Royal Astronomical Society, 465, 2616, doi: [10.1093/mnras/stw2870](https://doi.org/10.1093/mnras/stw2870)

Meneghetti, M. 2021, Lecture Notes in Physics, Vol. 956, Introduction to Gravitational Lensing: With Python Examples (Cham: Springer International Publishing), doi: [10.1007/978-3-030-73582-1](https://doi.org/10.1007/978-3-030-73582-1)

Miller, L., Kitching, T. D., Heymans, C., Heavens, A. F., & Van Waerbeke, L. 2007, Monthly Notices of the Royal Astronomical Society, 382, 315, doi: [10.1111/j.1365-2966.2007.12363.x](https://doi.org/10.1111/j.1365-2966.2007.12363.x)

Miller, L., Heymans, C., Kitching, T. D., et al. 2013, Monthly Notices of the Royal Astronomical Society, 429, 2858, doi: [10.1093/mnras/sts454](https://doi.org/10.1093/mnras/sts454)

Navarro, J. F., Frenk, C. S., & White, S. D. M. 1997, ApJ, 490, 493, doi: [10.1086/304888](https://doi.org/10.1086/304888)

Peebles, P. J. E. 1969, ApJ, 155, 393, doi: [10.1086/149876](https://doi.org/10.1086/149876)

Rowe, B. T. P., Jarvis, M., Mandelbaum, R., et al. 2015, Astronomy and Computing, 10, 121, doi: [10.1016/j.ascom.2015.02.002](https://doi.org/10.1016/j.ascom.2015.02.002)

Schneider, P., van Waerbeke, L., Jain, B., & Kruse, G. 1998, MNRAS, 296, 873, doi: [10.1046/j.1365-8711.1998.01422.x](https://doi.org/10.1046/j.1365-8711.1998.01422.x)

Shuntov, M., Akins, H. B., Paquereau, L., et al. 2025, arXiv e-prints, arXiv:2506.03243, doi: [10.48550/arXiv.2506.03243](https://doi.org/10.48550/arXiv.2506.03243)

Starikova, S., Jones, C., Forman, W. R., et al. 2014, ApJ, 786, 125, doi: [10.1088/0004-637X/786/2/125](https://doi.org/10.1088/0004-637X/786/2/125)

Tang, X.-x., Wang, P., Rong, Y., et al. 2025, arXiv preprint arXiv:2508.13597

Tovmassian, H. M. 2015, Astrophysics, 58, 328, doi: [10.1007/s10511-015-9387-4](https://doi.org/10.1007/s10511-015-9387-4)

Umetsu, K. 2020, The Astronomy and Astrophysics Review, 28, 7, doi: [10.1007/s00159-020-00129-w](https://doi.org/10.1007/s00159-020-00129-w)

Umetsu, K., Sereno, M., Lieu, M., et al. 2020, ApJ, 890, 148, doi: [10.3847/1538-4357/ab6bca](https://doi.org/10.3847/1538-4357/ab6bca)

Voges, W., Aschenbach, B., Boller, T., et al. 1999, A&A, 349, 389, doi: [10.48550/arXiv.astro-ph/9909315](https://doi.org/10.48550/arXiv.astro-ph/9909315)

Wang, L., Yang, X., Shen, S., et al. 2014, Monthly Notices of the Royal Astronomical Society, 439, 611, doi: [10.1093/mnras/stt2481](https://doi.org/10.1093/mnras/stt2481)

Xu, W., Shan, H., Li, R., et al. 2021, ApJ, 922, 162, doi: [10.3847/1538-4357/ac1b9e](https://doi.org/10.3847/1538-4357/ac1b9e)

Yang, X., Mo, H. J., Van Den Bosch, F. C., & Jing, Y. P. 2005, Monthly Notices of the Royal Astronomical Society, 356, 1293, doi: [10.1111/j.1365-2966.2005.08560.x](https://doi.org/10.1111/j.1365-2966.2005.08560.x)

Yang, X., Mo, H. J., Van Den Bosch, F. C., et al. 2007, The Astrophysical Journal, 671, 153, doi: [10.1086/522027](https://doi.org/10.1086/522027)

Yang, X., Mo, H. J., van den Bosch, F. C., Zhang, Y., & Han, J. 2012, ApJ, 752, 41, doi: [10.1088/0004-637X/752/1/41](https://doi.org/10.1088/0004-637X/752/1/41)

Yershov, V. N. 2014, Ap&SS, 354, 97, doi: [10.1007/s10509-014-1944-5](https://doi.org/10.1007/s10509-014-1944-5)